PCCP

ROYAL SOCIETY OF CHEMISTRY

PAPER

View Article Online
View Journal | View Issue

Check for updates

Cite this: *Phys. Chem. Chem. Phys.*, 2024, **26**, 28628

Received 8th July 2024,
Accepted 7th October 2024

DOI: 10.1039/d4cp02699c

rsc.li/pccp

Water adsorption at the (010) and (101) surfaces of $CuWO_4$†

Xuan Chu,[a] David Santos-Carballal*[a] and Nora H. de Leeuw*[ab]

Copper tungstate ($CuWO_4$) has attracted significant attention over the past two decades. However, the adsorption of water onto $CuWO_4$, which plays a critical role in the photocatalytic water splitting process, has not been investigated in detail. In this study, we have employed density functional theory (DFT) calculations to investigate water adsorption onto the $CuWO_4$ pristine (010) and reduced (101) surfaces. Surface phase diagrams as a function of temperature and partial pressure of H_2O were also constructed to determine water coverage under particular environmental conditions. Our study provides a comprehensive understanding of the adsorption of water on the major $CuWO_4$ surfaces, which is an important preliminary step in our investigation of photocatalytic water splitting over $CuWO_4$.

1. Introduction

The depletion of fossil fuels and accumulation of atmospheric CO_2 is a global challenge, simultaneously causing an international energy shortage and climate change.[1] Solar energy, an inexhaustible, sustainable, and decentralized natural energy resource, is a suitable alternative for coal, oil, and natural gas.[2] However, the approximately 10^5 terawatts per year (TW $year^{-1}$) of sun radiation on the surface of the Earth, which far exceeds current global needs of about 30 TW $year^{-1}$, has not been utilized comprehensively owing to the key challenges of solar energy harvesting and storage.[3] Since publication of the well-known Honda–Fujishima effect of TiO_2 in 1972,[4] photocatalytic water splitting, which provides a promising route to convert and store solar energy into a carbon-neutral H_2 fuel, has attracted increasing attention.[5–9]

In order to achieve industrial-scale utilization of photocatalytic water splitting to generate H_2, we first need to gain understanding of the interaction between the water molecules and the catalytic surfaces. Water has a complex structure when it interacts with a surface and is capable of forming 2-dimensional structures as well as 3-dimensional cage-like structures.[10–13] Several reviews have mentioned that the anomalies and unique nature of water are primarily due to the tetrahedral organisation of hydrogen-bonding.[14–16] It is widely accepted that one of the key challenges of modelling H_2O–surface interactions are the high fluctuations of the extensive H-bond networks.[17–19]

Metal oxides, such as TiO_2,[20] ZnO,[21] and WO_3,[22] have been employed in photocatalytic water splitting. However, TiO_2 has a relatively large bandgap of 3.2 eV, which leads to a narrow range of visible light absorption,[20] whereas ZnO suffers severely from a high rate of charge recombination.[21] WO_3 has poor chemical stability under either neutral or acidic conditions, although it exhibits a high electron diffusion length and mobility.[22] Recently, copper tungstate ($CuWO_4$), an n-type semiconductor, has attracted increasing interest as a potential photocatalyst for the water splitting process to generate and store H_2, owing to its earth abundancy, non-toxicity, and suitable bandgap of 2.4 eV.[23–26] Various studies have provided a comprehensive understanding of $CuWO_4$ as to its crystal morphology,[27] redox properties of the surface,[28] physiochemical properties,[29] and photocatalytic potential.[30–37] The conventional $CuWO_4$ unit cell is composed of two CuO_6 octahedral and WO_6 octahedral structures with shared zigzag oxygen chains. The bulk material has triclinic $P\bar{1}$ symmetry due to the Jahn–Teller effect, which breaks the Cu 3d e_g orbital degeneracy. Our previous study has shown that the valence band is mainly composed of O 2p states mixed with Cu 3d states, which are located between −6.5 and −4 eV. The conduction band, which comprises Cu 3d states mixed with O 2p and W 5d levels, lies between 2.3 and 3.1 eV. The calculated bandgap of the bulk $CuWO_4$ is 2.3 eV, which is consistent with the experimental result.[28] The structural and electronic properties of all 7 low-Miller index surfaces of $CuWO_4$ have been discussed in our previous work.[28]

In this study, we have carried out calculations based on the density functional theory (DFT) to predict the interaction of water with the pristine (010) and reduced (101) $CuWO_4$ surfaces.

---

[a] *School of Chemistry, University of Leeds, Leeds LS2 9JT, UK. E-mail: cmxch@leeds.ac.uk, d.santos-carballal@leeds.ac.uk*

[b] *Department of Earth Sciences, Utrecht University, Princetonplein 8A, 3584 CD Utrecht, The Netherlands. E-mail: n.h.deleeuw@leeds.ac.uk*

† Electronic supplementary information (ESI) available. See DOI: **https://doi.org/10.1039/d4cp02699c**

The structural and electronic properties of the hydrated systems, including bond lengths, adsorption energies, charge transfer, vibrational frequencies of H_2O, and the work functions, were calculated to characterize and evaluate the different adsorption modes. The phase diagrams of the two surfaces have also been obtained as a function of temperature and partial pressure of H_2O to determine the coverage of the surface under specific conditions. Our study aims to provide a comprehensive understanding of the interaction of water with $CuWO_4$ surfaces and guide future studies in utilizing this material for the photocatalytic splitting of water, where adsorption is necessarily the first step in the process before water dissociation and catalytic conversion into hydrogen and oxygen can take place.

2. Computational details

2.1 DFT calculations

In this work, we performed DFT calculations using the Vienna ab initio simulation package (VASP).[38,39] The core states of Cu: [Ar], W: [Xe], O: [He], and their interactions with the valence orbitals were treated using the projector augmented wave (PAW) formalism,[40] whereas their remaining electrons and that of the H atom was treated as valence electrons. The Perdew–Burke–Ernzerhof (PBE) functional was employed to calculate the exchange–correlation energy.[41] The long-range component of the van der Waals interactions was corrected using the D3 method with Becke–Johnson damping.[42] We used periodic plane wave basis sets with a cut-off energy of 400 eV for the expansion of the Kohn–Sham valence states. The energy cutoff was tested from 400 to 800 eV, but as the effect on energy differences was negligible, we have selected 400 eV for all our calculations. We applied the DFT+U method to correct the electronic self-interaction in the transition metal d orbitals caused by the pure GGA functionals.[43] We tested the onsite Coulomb interaction term (U_{eff})[44] for both cations between 3 and 10 eV, and found that only Cu needs this correction. We selected U_{eff} = 7.5 eV, as this value provides the best description of the lattice parameters and the bandgap with respect to the experimental data. Our tests suggested that the U correction is unnecessary for the W atoms since they lose all their d electrons upon formation of $CuWO_4$. An alternative way to accurately describe the electronic properties of transition metal compounds is through the use of hybrid functionals. However, this method requires significantly more computational resources compared to DFT+U when applied to a surface model. Thus, we have opted in this work to follow the DFT+U approach, as it has shown to work well for our material.[28] The bulk material was modelled using the triclinic primitive unit cell containing 12 atoms ($Cu_2W_2O_8$), which was sampled in the reciprocal space using a Γ-centered 4 × 3 × 4 k-points mesh.[45] The isolated H_2O molecule was modelled in an 8 × 8 × 8 $Å^3$ periodic box to avoid the influence of images in adjacent simulation cells, where only the Γ point was sampled. We have used the conjugate gradients algorithm to optimize the geometries of the surfaces until the Hellmann–Feynman forces on each atom were smaller than 10^{-2} eV $Å^{-1}$ and the energy difference between consecutive steps of the self-consistent loop was below 10^{-6} eV.[46]

2.2 Surface models

In this study, we used the dipole method proposed by Tasker to construct the pristine low-Miller index (010), (101), and (110) surfaces.[47] This method creates surfaces in such a way that no dipole moment exists perpendicular to the surface. The method considers the crystal as a stack of planes, which can be classified into three types. In type 1, each plane has no net charge, as it is composed of cations and anions in stoichiometric ratio, which makes the surface non-polar. In type 2, an integer number of formula units is contained within several charged layers, which are stacked in a symmetric fashion that cancels the dipole moment. In type 3, there is a dipole moment perpendicular to the surface due to the non-symmetric stacking of the charged planes. Type 3 surfaces require reconstruction by moving half of the ions with the same charge from the top-most slab layer to the bottom-most to form non-polar surfaces. We employed the METADISE package to construct the low-Miller index surfaces from the bulk phase of $CuWO_4$.[48] A 10 Å vacuum was introduced perpendicular to the surface to prevent the interaction between the periodically repeated images of the $CuWO_4$ slab and to allow space to adsorb the H_2O molecules. The 2 × 2 × 1 supercells were employed to build the pristine (010), reduced (101) and oxidized (110) surfaces, which were generated from the bulk $CuWO_4$. We used the surface slabs composed of 16 Cu atoms, 16 W atoms and 64 O atoms for the pristine (010) surface; 32 Cu atoms, 32 W atoms, 124 O atoms for the reduced (101) surface; and 32 Cu atoms, 32 W atoms, 143 O atoms for the oxidized (110) surface. The topmost 2 layers of each slab are allowed to relax during the optimization, while the bottommost 2 layers were kept fixed at their bulk-optimised positions. For the appropriate sampling of the Brillouin zone, we tested different Monkhorst–Pack k-point meshes for the low-Miller index surfaces.[45] We used a 2 × 2 × 1 k-point mesh for the three surfaces. For the geometry optimisations and to obtain accurate energies, we applied the tetrahedron method with Blöchl correction for the bulk and surfaces, and Gaussian smearing for the isolated H_2O molecule to account of the electron partial occupancies.[49]

To create the reduced (101) surface, we removed one O atom from the topmost layer of the pristine surface. The oxidized (110) surface was modelled by adding three O atoms sequentially to the exposed cations with dangling bonds in the topmost surface layer. The structures of both the partially reduced and partially oxidized surfaces were fully relaxed, and the atomic configuration with the lowest surface free energy was selected for the next addition of O adatoms or O vacancies.

The surface energies of the slabs before (γ_u) and after (γ_r) relaxation were defined as:[28,50]

$$\gamma_u = \frac{E_u - nE_b}{2A} \tag{1}$$

$$\gamma_{\mathrm{r}} = \frac{E_{\mathrm{r}} - nE_{\mathrm{b}}}{A} - \gamma_{\mathrm{u}} \tag{2}$$

where E_u, E_r, and E_b are the energies of the unrelaxed slab, half-relaxed slab, and one formula unit in the bulk, respectively. A represents the area of the slab and n is the number of formula units in the slab.

The H_2O adsorption process on the pristine and reduced surfaces of one formula unit of $CuWO_4$ can be described by reactions (3) and (4) respectively.

$$\mathrm{CuWO_4(s)} + n\mathrm{H_2O(g)} \rightarrow \mathrm{CuWO_{4+\mathit{n}}H_{2\mathit{n}}(s)} \tag{3}$$

$$\mathrm{CuWO_3(s)} + n\mathrm{H_2O(g)} \rightarrow \mathrm{CuWO_{3+\mathit{n}}H_{2\mathit{n}}(s)} \tag{4}$$

Based on the reactions, the surface free energy ($\sigma_{ads}(T, p)$) of the $CuWO_4$ surfaces in thermodynamic equilibrium with ideal gas phase H_2O is defined as:

$$\sigma_{\mathrm{ads}}(T,p) = \gamma_{\mathrm{r}} + C\left(\frac{E_{\mathrm{sys}} - E_{\mathrm{r}} - n\left(E_{\mathrm{H_2O}} - TS_{\mathrm{H_2O}}\left(T, p^0_{\mathrm{H_2O}}\right)\right)}{n} - RT\ln\frac{p_{\mathrm{H_2O}}}{p^0_{\mathrm{H_2O}}}\right) \tag{5}$$

where $C = \frac{n}{A}$ represents the surface coverage of the H_2O molecules, n is the number of H_2O molecules adsorbed on the surface, and E_{sys} and E_{H_2O} are the relaxed energies of the $CuWO_4$ surface slab with the adsorbed H_2O molecules and the energy of an isolated H_2O molecule, respectively. $S_{H_2O}(T, p^0)$ represents the entropy of gas H_2O in the standard state taken from the thermodynamic tables,[50] p_{H_2O} is the partial pressure of H_2O, T is the temperature, and R represents the ideal gas constant. VASPKIT was also used for calculating the entropy of water from 100 to 2000 K for the sake of validation.

In this work, chemisorption refers to water adsorption which involves dissociation of the water molecule and electronic structure changes leading to the formation of bonds, whereas the water molecule remains intact in physisorption which does not result in changes in the chemical bonding. The adsorption energy (E_{ads}) of the H_2O molecule on the $CuWO_4$ surface is defined as:[51]

$$E_{\mathrm{ads}} = E_{\mathrm{sys}} - E_{\mathrm{r}} - nE_{\mathrm{H_2O}} \tag{6}$$

We have also calculated the variation of the Helmholtz free energy, considering whether the zero-point energy and the vibrational contribution of the entropy at 298 K have an impact on the energies. However, as shown in Table S1 (ESI†) such impact is negligible, and we have therefore only focussed on the energies of the adsorption system at 0 K.

We calculated the atomic Bader charges and atomic magnetic moments *via* an improved grid-based algorithm.[52,53] The work function (Φ), which is defined as the minimum thermodynamic energy required to remove one electron from the Fermi level (E_F) at the $CuWO_4$ surface to the vacuum level (E_{vac}), was obtained by the following equation:[28]

$$\Phi = E_{\mathrm{vac}} - E_{\mathrm{F}} \tag{7}$$

The charge difference ($\Delta\rho$) of the surface before (ρ_{CuWO_4}) and after adsorption of H_2O ($\rho_{CuWO_4+H_2O}$) was defined as:[54]

$$\Delta\rho = \rho_{\mathrm{CuWO_4+H_2O}} - \rho_{\mathrm{CuWO_4}} - \rho_{\mathrm{H_2O}} \tag{8}$$

where ρ_{H_2O} represents the charge density of the isolated H_2O molecule. All the charge densities were obtained at the same geometry as the adsorption system.

We used the Tersoff–Hamann approach to simulate scanning tunnelling microscopy (STM) images, where the tunnelling current is proportional to the local density of states (LDOS) of the surface at the position of the tip integrated between the Fermi level and the applied bias.[55] The HIVE program was used to generate the STM images.[56]

3. Results and discussion

3.1 Isolated H_2O molecule

We first modelled and calculated the electronic properties of an isolated H_2O molecule. Table 1 lists the calculated bond distances (d), bond angles ($\angle$), and the unscaled and scaled asymmetric stretching (υ_{asym}), symmetric stretching (υ_{sym}) and bending (δ) fundamental vibrational modes for the isolated H_2O molecule. The results suggest that our simulation of the equilibrium bond distances as well as the bond angle are in good agreement with the experimental data.[56] We have calculated the harmonic vibrational modes as the second derivative of the potential energy with respect to the atomic position in the vicinity of the minimum of the well *via* the finite differences approach, where a positive and negative displacement of 0.015 Å is allowed for each ion in each Cartesian direction to calculate the Hessian matrix. The unscaled asymmetric stretching and symmetric stretching harmonic vibrational mode are red-shifted by 176 and 162 cm^{-1}, respectively, whereas the bending harmonic vibrational mode is blue-shifted by 31 cm^{-1} compared to experiments.[57,58] However, experimental vibrational modes represent transitions between the ground state and the first vibrational energy level of an anharmonic potential energy surface. Thus, we obtained the empirical factor c = 0.96 to scale our vibrational modes and make them directly comparable to the anharmonic system.[50] The scaling factor was

Table 1 Bond distances (d), bond angles ($\angle$), as well as unscaled and scaled asymmetric stretching (υ_{asym}), symmetric stretching (υ_{sym}) and bending (δ) fundamental vibrational modes for H_2O

Properties	Calculated		Experiment
d (Å)	0.972		0.958[56]
$\angle$ (°)	104.40		104.48[56]
	Unscaled	Scaled	
υ_{asym} (cm^{-1})	3932	3781	3756[57]
υ_{sym} (cm^{-1})	3819	3672	3657[57]
δ (cm^{-1})	1564	1504	1595[58]

calculated as:

$$c = \frac{\sum \omega_{\text{exp}}\omega_{\text{calc}}}{\sum {\omega_{\text{calc}}}^2} \quad (9)$$

where ω_{exp} and ω_{calc} represent the experimental and calculated harmonic vibrational wavenumbers, respectively. The results indicate that differences of only 25 and 15 cm^{-1} were obtained in the scaled asymmetric and symmetric stretching vibrational modes, respectively, compared to experimental data.[57] However, the scaled bending mode was underestimated by 91 cm^{-1} compared to the experimental data.[58]

3.2 Crystal morphology of $CuWO_4$

To determine the most suitable surfaces for water adsorption, we derived the Wulff crystal morphology of $CuWO_4$ from the Miller index surfaces with the lowest surface free energies. In our previous work, we have studied the redox properties of the low-Miller index surfaces under the working conditions of the gas phase water splitting process.[28] The Wulff construction of the equilibrium morphology is obtained from equation $\frac{\sigma_1}{d_1} = \frac{\sigma_2}{d_2} = \cdots = \frac{\sigma_n}{d_n} = c$, where σ and d represent the surface free energy of the surface and the distance of the surface from the centre of the crystal, respectively, and c is a constant. In our previous study,[28] we have shown that under the working conditions of gas phase water splitting, *i.e.* 298 K, the (010) surface stayed pristine, whereas the (101) surface was reduced with a surface coverage of −2.5 nm^{-2} and the (110) surface was oxidized at 700 K. The equilibrium morphologies of $CuWO_4$ at 298 K and 700 K are shown in Fig. 1a and Fig. S1 (ESI†), respectively. Note that we have ignored possible structural changes caused by thermal expansion of the material, as they are beyond the scope of this work and are likely to be negligible at the temperatures considered in this work. The pristine (010) surface dominates the morphology owing to its lowest surface free energy of 36 meV Å^{-2} under working conditions, as shown in the orange region in Fig. 1a. The reduced (101) surface is the second predominant facet expressed under working conditions with a surface free energy of 56 meV Å^{-2}, shown in blue in Fig. 1a. The reduced (101) surface is characterised by one O atom vacancy, corresponding to a coverage of O vacancies of 2.5 nm^{-2}. The dominance of these two surfaces prevents the expression of the (100) and (111) surfaces, resulting in an equilibrium morphology with a dodecahedron shape consisting of 4 hexagons, 4 pentagons and 4 quadrilaterals. The oxidized (110) surface with a surface free energy of 19 meV Å^{-2} is also expressed when the temperature reaches 700 K, as shown in Fig. S1 (ESI†). However, the result suggests that the water molecule is not capable to chemisorb at the oxidized (110) surface due to the occupation of the adsorption sites by O atoms. Tests of water physisorption show negligible interactions. Thus, we do not consider further the oxidized (110) surface in the following discussions.

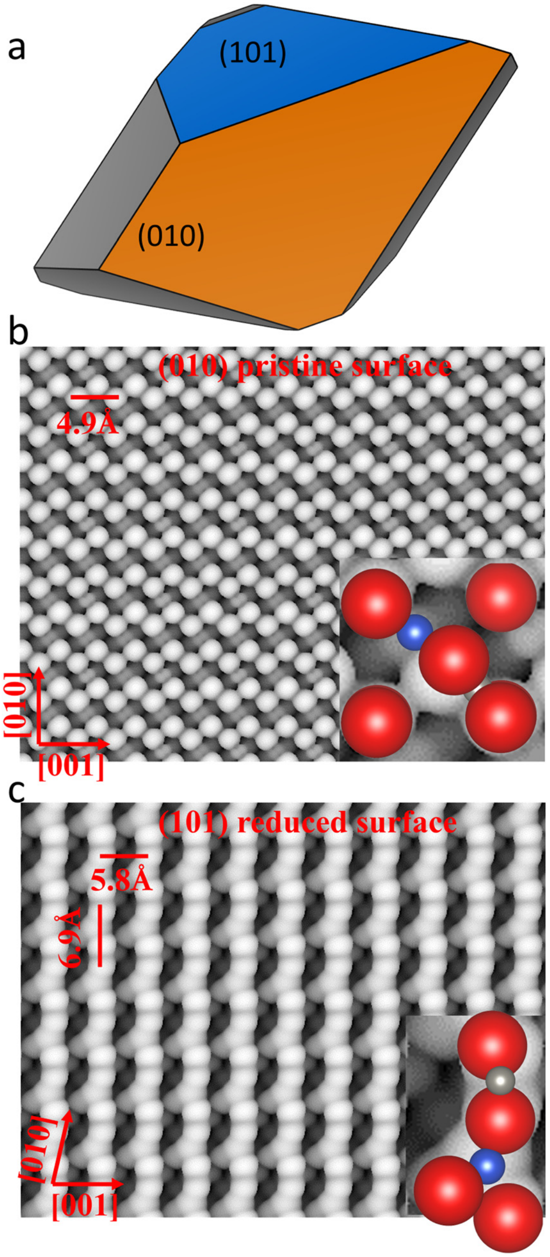

Fig. 1 (a) Equilibrium Wulff morphology of $CuWO_4$ at 298 K and scanning tunnelling microscopy (STM) images of (b) the pristine (010) and (c) the reduced (101) surfaces of $CuWO_4$. Cu, W, and O atoms are shown as blue, grey, and red, respectively.

We simulated the STM images of the optimized pristine (010) and reduced (101) surfaces of $CuWO_4$, as illustrated in Fig. 1b and c. The STM image of the pristine (010) surface was acquired at a distance (d) of 1.5 Å from the tip and at a density (ϱ) of 0.008e Å^{-3}. The 4-fold Cu cations of the topmost layer were resolved as dark spots, whereas five O anions of the CuO_6 and WO_6 octahedral units appear as bright spots. The W cations, which are linking two O anions, are not shown in the STM image due to their low partial charges at the sample bias of −1.5 eV. The STM image of the pristine (010) surface suggests that the 4-coordinated Cu cations in the top layer of the surface can potentially act as adsorption sites for the H_2O molecule owing to their two dangling bonds. The STM image of the reduced (101) surface was simulated at a distance of 1.8 Å from the tip and at a density of 0.003 e Å^{-3} using a sample bias of −3.0 eV. The STM image of the reduced (101) surface suggests that the 3-coordinated Cu cations and 4-coordinated W cations in the topmost layer of the slab, which are shown as bright spots, can potentially act as adsorption sites for H_2O owing to their dangling bonds.

3.3 Single water molecule adsorption

In the initial adsorption structures, we sited the H_2O molecule above each potential adsorption site at 2 Å away from the surface, with the O atom coordinating the undercoordinated metal cation and with the H atoms interacting with the O anion exposed in the topmost layer of the surface. For a better description of the adsorption configurations of the H_2O molecule, we have employed a notation widely used in organometallic chemistry, which is based on the hapticity of the ligands (μ_n) and the number of surface atoms it can bridge (η^m).[59–61]

3.3.1 Pristine (010) surface. On the pristine (010) surface, the Cu and W cations and the O anion from the topmost layer were tested as potential sites for the adsorption of a single H_2O molecule. The fully optimized structures of the most stable adsorption modes are illustrated in Fig. 2, and their electronic properties are listed in Table 1.

We found that H_2O coordinated molecularly the topmost surface Cu atom, forming a μ_1–η^1 configuration as illustrated in Fig. 2a. The O atom of the H_2O molecule (O_w) was oriented towards the surface to restore the octahedral coordination of CuO_6. The Cu–O_w bond distance was 2.05 Å, which is consistent with the length of the Cu–O bond (1.95–2.40 Å) in the bulk phase. The hydrogen atoms, on the other hand, pointed outwards from the surface, which indicates that no hydrogen bond is formed between the H_2O and the O of the surface (O_s). The surface exhibited negligible structural distortion after relaxation, except that the Cu of the adsorption site was displaced outwards by 0.22 Å, due to the Coulomb attraction of O_w. As listed in Table 2, E_{ads} of the single H_2O adsorption system was calculated as −0.69 eV, which was attributed to the formation of the Cu–O_w bond. As listed in Table 2, the charge density difference (Δq) of this adsorption mode suggests that a minor electron density of 0.10e migrated from the adsorbed H_2O molecule to the surface. We highlighted the atoms with the largest atomic charge transfer in the right panels of Fig. 2. The results suggest that a strong polarisation of the H_2O molecule occurred during adsorption onto the $CuWO_4$(010) surface which caused a charge redistribution. As a result, 0.81 e of O_w migrated to the two H, which gained 0.34 and 0.37 e, whereas the O_s gained 0.1 e. The work function of the hydrated system was calculated at 6.15 eV, which is 0.80 eV lower than the dry surface, revealing that the former can provide electron charge more easily than the latter. We calculated the vibrational modes of the adsorbed water molecule, listed in Table 2. For the hydrated (010) surface, the asymmetric and symmetric stretching modes of the H_2O molecule are red-shifted by 131 and 153 cm^{-1} with respect to the isolated molecule, which indicates that the O_wH bond became weaker during adsorption. On the other hand, the bending mode was red-shifted by only 45 cm^{-1} compared to the isolated water molecule.

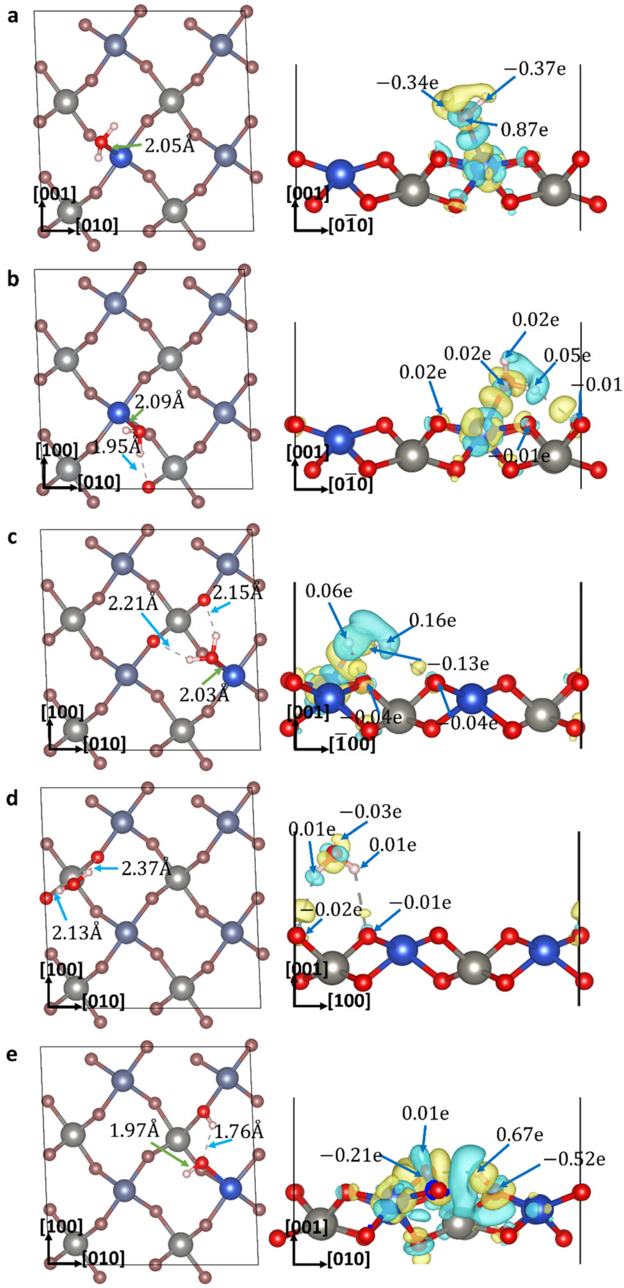

Fig. 2 (left panels) Top view of the most stable adsorption modes of a single H_2O molecule on the pristine (010) surface of $CuWO_4$: molecular adsorptions (a) μ_1–η^1 on Cu site, (b) μ_2–η^2 on Cu site, (c) μ_3–η^3 on Cu site, (d) μ_2–η^2 on O site, and (e) dissociative adsorption μ_2–η^2 on Cu site. The length of the ionic bonds (green arrow) and hydrogen bonds (blue arrow) are noted. The Cu, W, and O atoms are shown as blue, grey, and red, respectively. Dark blue Cu atoms indicate the H_2O adsorption sites. (right panels) Side view of the charge density differences caused by the water adsorption. Yellow regions represent electron gain, whereas blue regions represent electron loss. Crystallographic directions are indicated by numbers within brackets.

Table 2 Binding configurations, adsorption energies (E_{ads}) at 0 K, bond lengths (*d*), charge transfers (Δq),work function (Φ) and vibrational wavenumbers for the asymmetric stretching (υ_{asym}), symmetric stretching (υ_{sym}), and bending (δ) modes of a single H_2O molecule adsorbed at different sites of the pristine (010) surface. The positive and negative values of Δq represent charge gained and lost, respectively, by H_2O during adsorption

	Molecular				Dissociative
Site	Cu	Cu	Cu	O	Cu
Configuration	μ_1–η^1	μ_2–η^2	μ_3–η^3	μ_2–η^2	μ_2–η^2
E_{ads} (eV)	−0.69	−0.69	−0.89	−0.26	−0.12
d O–metal (Å)	2.05	2.09	2.03		1.97
d H bond$_1$ (Å)		1.95	2.15	2.13	1.76
d H bond$_2$ (Å)			2.21	2.37	
Δq (*e*)	0.10	0.09	0.10	−0.02	0.47
Φ (eV)	6.15	6.28	6.45	6.54	6.48
υ_{asym} (cm^{-1})	3650	3600	3475	3614	3727
υ_{sym} (cm^{-1})	3519	3281	3396	3517	3352
δ (cm^{-1})	1459	1541	1510	1544	

The H_2O molecule is also capable of forming a μ_2–η^2 configuration when adsorbing onto Cu, as illustrated in Fig. 2b. The Cu–O_w bond with a length of 2.09 Å is oriented towards the surface to maintain the octahedral coordination of CuO_6 in the bulk phase, whereas the O_wH group formed a 1.95 Å long hydrogen-bond with O_s. The Cu migrated outward slightly due to the Coulomb attraction of O_w, but the rest of the slab atoms stayed at their relaxed dry surface positions. The adsorption energy is −0.69 eV, which is identical to the value calculated for the configuration in the absence of hydrogen-bonds, discussed previously. The result suggests that hydrogen-bonds do not play a major role in the thermodynamics of these adsorption configurations. As illustrated in the right panel of Fig. 2b, a small charge density of 0.09*e* transferred from the H_2O molecule to the surface. The O_w donated 0.02 *e* to the Cu adsorption site. The two H atoms provided 0.02 and 0.05 *e* to the surface, as illustrated in Fig. 2b. The work function increased to 6.28 eV compared to the adsorption configuration without hydrogen-bond, which is still 0.67 eV smaller than the dry surface, suggesting that the hydrated catalyst surface is better capable of providing electron charge when facilitating chemical reactions. Table 2 lists our estimated asymmetric (3600 cm^{-1}) and symmetric (3281 cm^{-1}) stretching modes, which are red-shifted by 181 and 391 cm^{-1}, respectively, compared to the isolated water molecule. Our results suggest that the intramolecular OH bonds become weaker during adsorption. The estimated bending mode was over 1541 cm^{-1}, which was only 37 cm^{-1} larger than for the isolated water molecule.

We also tested the physisorption of water molecule onto O_s. However, the H_2O molecule chemisorbed onto the nearest Cu cation after optimization, forming a μ_3–η^3 configuration as indicated in Fig. 2c. The calculated bond distance for Cu–O_w was 2.03 Å, which is in good agreement with the length of the Cu–O bond in the bulk phase. The Cu–O_w bond oriented towards the surface to maintain the octahedral geometry of CuO_6. Additionally, H_2O formed two hydrogen-bonds with O_s at 2.15 and 2.21 Å, which forced the molecular plane of the adsorbate to lie approximately parallel to the surface, as illustrated in Fig. 2c. The surface did not suffer major structural distortions as only the Cu adsorption site migrated outwards slightly due to the Coulomb attraction of O_w. The E_{ads} of this adsorption configuration was −0.89 eV, which is the most favourable adsorption mode for the pristine $CuWO_4$(010) surface. The result also suggests that chemisorption of the water molecule at the Cu is the primary interaction on the pristine (010) surface, whereas physisorption on O_s can only be considered as a secondary interaction. As listed in Table 2, the Δq of this adsorption structure shows that an electron charge of 0.1 *e* migrated to the surface after optimization, whereas the polarization of the H_2O molecule was also observed. The two H atoms contributed 0.06 and 0.16 *e* to the O_w (gained 0.13 *e*) and two O_s (gained 0.04 *e*) to form a Cu–O_w coordination bond and hydrogen-bonds, and 0.02 migrated to the other anions of the surface, as illustrated in the right panel of Fig. 2c. The calculated work function for this hydrated surface was 6.45 eV, which is 0.5 eV smaller than the dry surface, suggesting that the hydrated system is better at providing electron charge and facilitating chemical reactions. As listed in Table 2, the symmetric and asymmetric stretching modes were estimated at 3396 and 3475 cm^{-1}, respectively, which are significantly red-shifted compared to the isolated water molecule, suggesting that the intramolecular OH bonds become weaker after adsorption. The estimated bending mode lies at 1510 cm^{-1}, which is only 5 cm^{-1} different from the isolated water molecule.

We did not find any configuration where O_w interacted with W, since this atom has no dangling bond available in the topmost surface layer. Whereas the Cu atoms in the topmost layer of the pristine (010) surface have lost their two O ligands, which has created two dangling bonds available for the adsorption of the H_2O molecule, the W atoms in the topmost layer of the pristine (010) surface maintained their WO_6 octahedral coordination. The STM images plotted in Fig. 1b also show that the W atoms are shielded by two O atoms and as such, they are not able to bind the O atom of the H_2O molecule.

As illustrated in Fig. 2d, the H_2O molecule interacts with O_s *via* two hydrogen-bonds at 2.13 and 2.37 Å, forming a μ_2–η^2 configuration. The molecular plane of H_2O was perpendicular to the surface but the O_w moved outwards due to the Coulomb repulsion of the O_s. The structure of the surface did not change noticeably after relaxation because of the relatively weak hydrogen-bond interactions. The E_{ads} of this adsorption pattern was −0.26 eV, which was mainly attributed to the two hydrogen-bonds. The surface lost a negligible electron density of 0.02 *e* to the H_2O molecule, whereas the main electronic effect was the polarization of the water molecule. As illustrated in Fig. 2d, the O_w anion gained 0.03 *e* from the surface and H, and two O_s gained 0.01 and 0.02 *e* to form H-bonds. The calculated work function of the simulated system was 6.54 eV, which is 0.41 eV smaller than that of the dry surface. The result indicates that the hydrated surface will more easily donate electron charge which improves the chemical reactivity. The calculated symmetric and asymmetric stretching modes of the adsorbed water were 3518 and 3614 cm^{-1}, *i.e.* red-shifted by 155 and 167 cm^{-1}, respectively, compared to the isolated water molecule, indicating that the intramolecular OH bonds become weaker after adsorption, as listed in Table 2. The bending mode was estimated at 1544 cm^{-1}, which increased slightly by 40 cm^{-1} compared to the isolated water molecule.

We also obtained a single dissociatively adsorbed H_2O molecule with a μ_2–η^2 coordination geometry, as presented in Fig. 2e. It is worth noting that the dissociation of water discussed in this study occurred spontaneously upon adsorption of water at the surface and the dissociative process is therefore treated as barrierless. The O_wH group coordinating the exposed Cu on the surface, has a bond length of 1.97 Å and a bond angle $\angle HO_wCu$ of 113.43°. The dissociated H atom formed a hydroxyl group with a surface O_s atom. We also found that the O_sH group formed a hydrogen-bond at 1.76 Å to O_wH. The surface exhibited negligible structural distortion except at the Cu adsorption site, where the Cu atom was pulled outward due to the Coulomb attraction of O_w. The E_{ads} for the dissociative single H_2O adsorption is −0.12 eV, which is smaller than for the molecular adsorption configuration. Releasing less energy indicates that water prefers to adsorb molecularly on the pristine (010) $CuWO_4$ surface. As listed in Table 2, the surface gained electron density of 0.47 *e* after hydration. We have shown the atoms with noticeable charge density differences in the panels on the right of Fig. 2e. The O_w gained 0.21 *e* from the surface and bonded H. The dissociated H atom contributed significantly by 0.67 *e* to form the O_sH bond, and the O_s obtained 0.52 *e* correspondingly. The work function for this hydrated system was 6.48 eV, *i.e.* 0.47 eV smaller than the dry surface, indicating that the former provides electron charge more easily, thereby improving the chemical reactivity. We calculated the vibrational stretching mode for the dissociative H_2O as listed in Table 2. For the O_wH group, it was estimated at 3727 cm^{-1}, which is blue-shifted by 55 cm^{-1} compared to the symmetric stretching mode, and red-shifted by 54 cm^{-1} compared to the asymmetric stretching mode. The result indicates that the strength of the O_wH bond did not change noticeably due to the slight difference in stretching modes compared to the isolated water molecule. The calculated stretching mode for the O_sH group was 3352 cm^{-1}, which is 320 and 429 cm^{-1} smaller than the symmetric and asymmetric stretching modes of the isolated water molecule, respectively.

3.3.2 Reduced (101) surface. We investigated the adsorption of a single H_2O molecule on the reduced (101) surface of $CuWO_4$. The metal Cu_a (in the topmost slab layer), Cu_b (in the sub-surface layer), W atom, and O atom were all considered as potential adsorption sites. The sub-layer W atoms were shielded by the top O atoms, and they were thus not considered as adsorption sites. The structure of each adsorption system is depicted in Fig. 3, and their electronic properties are listed in Table 3.

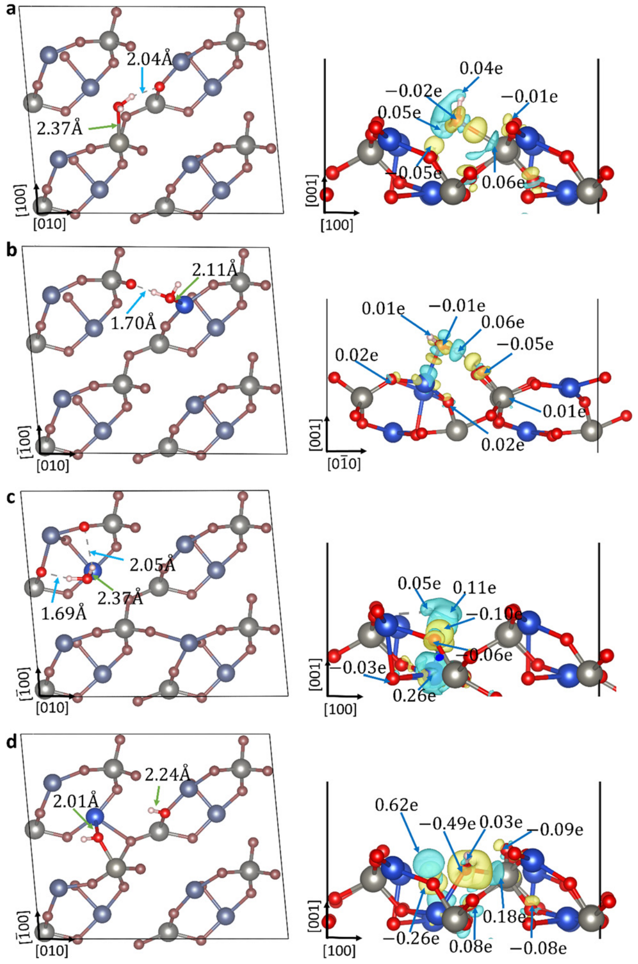

Fig. 3 (left panels) Top view of the most stable adsorption modes of a single H_2O molecule on the reduced (101) surface of $CuWO_4$: molecular adsorptions (a) μ_2–η^2 on Cu_a site, (b) μ_3–η^3 on Cu_b site, (c) μ_2–η^2 on W site, (d), and dissociative adsorption μ_3–η^3 on W site. The lengths of the ionic bonds (green arrow) and hydrogen bonds (blue arrow) are noted. The Cu, W, and O atoms are blue, grey, and red, respectively. Dark blue Cu atoms represent the H_2O adsorption sites; (right panels) side view of the charge density differences as a result of the adsorption compared with the dry (101) surface. The region coloured in light yellow represents charge gain (noted as positive value), whereas the region coloured in light blue represents charge loss (noted as negative value) after adsorption. Crystallographic directions are indicated by numbers within brackets.

As illustrated in Fig. 3a, the H_2O was able to adsorb molecularly on the W site in the topmost surface layer, forming a coordinate W–O bond with bond length of 2.37 Å. The O_w oriented towards the surface to keep the octahedral coordination geometry of the WO_6 in the bulk phase, complementing the μ_2–η^2 configuration with a hydrogen-bond to O_s. The length of the hydrogen-bond is 2.04 Å as noted in Fig. 3a. The surface suffered negligible structural change after adsorption except for slight outward displacement of the W due to the Coulomb attraction of O_w. The E_{ads} for this adsorption configuration is −0.81 eV, which is the thermodynamically most favourable adsorption mode for a single water molecule that we obtained at the reduced (101) $CuWO_4$ surface. The hydrated surface only gained electron charge of 0.06 *e* as listed in Table 3, whereas the polarization of the water molecule is also small. We have shown in the right panel of Fig. 3 the atoms with noticeable charge density difference after hydration. The O_w gained 0.02 *e*, partially provided by the W adsorption site with 0.06 *e* and two H atoms with 0.04 and 0.05 *e*. The O_s that interacted with

Table 3 Binding configurations, adsorption energies (E_{ads}) at 0 K, bond lengths (d), charge transfers (Δq), work functions (Φ) and vibrational wavenumbers for the asymmetric stretching (υ_{asym}), symmetric stretching (υ_{sym}), and bending (δ) modes of a single H_2O molecule adsorbed at different sites of the reduced (101) surface. The positive and negative values of Δq represent charge gained and lost, respectively, by H_2O during adsorption

	Molecular			Dissociative
Site	Cu_a	Cu_b	W	W
Configuration	μ_2–η^2	μ_3–η^3	μ_2–η^2	μ_3–η^3
E_{ads} (eV)	−0.63	−0.53	−0.81	−0.53
d O–Metal (Å)	2.11	2.05	2.37	2.01
d H bond$_1$ (Å)	1.70	1.69	2.04	
d H bond$_2$ (Å)		2.37		
$\Delta\rho$ (e)	0.06	0.07	−0.07	0.16
Φ (eV)	4.78	4.74	4.99	5.33
υ_{asym} (cm^{-1})	3616	3551	3597	3719
υ_{sym} (cm^{-1})	3173	2984	3281	3618
δ (cm^{-1})	1521	1537	1530	

the H atom gained 0.05 e when forming a hydrogen-bond. The four O atoms coordinating the W adsorption site gained 0.01 e in total after adsorption. The work function of the hydrated surface is 4.99 eV, which is 0.96 eV lower than the reduced (101) surface, indicating that the hydrated surface is significantly more reactive than the dry surface. The result is in good agreement with the increase in the charge density of the surface, discussed before. As listed in Table 3, the symmetric and asymmetric stretching modes of the adsorbed water were estimated at 3281 and 3598 cm^{-1}, which are red-shifted by 391 and 184 cm^{-1}, respectively, with respect to the isolated water molecule. Our results indicate that the intra-molecular OH bonds are weaker after adsorption. The bending mode changed slightly by 26 cm^{-1} compared to the isolated water molecule.

The H_2O was able to chemisorb at the Cu_a adsorption site, forming a μ_2–η^2 configuration, as shown in Fig. 3b. The length of the Cu_a–O_w bond is 2.11 Å, whereas the hydrogen-bond formed is 1.70 Å long. The Cu_a–O_w bond is oriented outwards to maintain the octahedral coordination of CuO_6 in the bulk phase, and the Cu at the adsorption site was pulled outwards due to the Coulomb attraction of the O_w. The E_{ads} for the adsorption system is −0.63 eV, which is smaller than the hydrated system discussed before, suggesting that the water molecule prefers to adsorb onto W. Electron density of 0.06 e migrated to the surface, as listed in Table 3. The O_w gained 0.01 e when it coordinated Cu, whereas the two H atoms contributed 0.01 and 0.06 e to O_w and the surface, respectively and the O_s gained 0.05 e after hydration. The work function of this system was calculated as 4.78 eV, which is 1.17 eV smaller than the dry reduced surface, revealing that the surface becomes significantly more reactive after hydration. The result is consistent with the electron density increase of the hydrated surface. The symmetric and asymmetric stretching modes are estimated at 3173 and 3616 cm^{-1} as listed in Table 3, which are red-shifted by 499 and 165 cm^{-1}, respectively. The result suggests that the intramolecular OH bonds become weaker after hydration. The bending mode is found at 1521 cm^{-1}, which is only a negligible change compared to the isolated water molecule.

Since the reduced (101) surface contains O vacancies, we investigated the adsorption of a single H_2O molecule at the exposed Cu_b of the sub-layer. As shown in Fig. 3c, the O_w was pushed towards the top layer of the surface to maintain the octahedral coordination of the CuO_6, bonding with Cu_b at 2.05 Å. Two hydrogen-bonds were established at 1.69 and 2.37 Å distance, interacting with O_s to complement the μ_3–η^3 adsorption configuration. The surface slab suffered negligible structural change after relaxation. The E_{ads} calculated for this adsorption mode is −0.53 eV, resulting in a weaker adsorption pattern than the two adsorption systems discussed previously. After hydration, 0.07 e electron density had migrated from the H_2O molecule to the surface, listed in Table 3. The O_w gained 0.1 e electron density, which was partially compensated by the Cu at the adsorption site that lost 0.26 e upon interaction with H_2O. Two H contributed 0.05 and 0.11 e, whereas two O_s gained 0.01 and 0.06 e owing to the formation of hydrogen-bonds. The work function was calculated at 4.74 eV, which is 1.21 eV smaller than for the dry surface, indicating that the surface becomes significantly more reactive upon hydration. The symmetric and asymmetric stretching modes became 2984 and 3551, listed in Table 3, which are red-shifted by 688 and 230 cm^{-1}, respectively, upon hydration. The result shows that the intramolecular OH bond becomes weaker compared to the isolated water molecule. However, the bending mode is slightly blue-shifted to 1538 cm^{-1} after hydration.

Dissociative adsorption of a single H_2O molecule also occurred at the reduced (101) surface, shown in Fig. 3d. The O_wH group, which was initially located at W in the top-layer of the surface, migrated and after optimisation bound the sub-surface Cu_b. The Cu_b–O_w and W–O_w bond lengths are 2.24 and 2.01 Å, respectively, and the dissociated H atom bound one O_s, completing a μ_3–η^3 configuration. The Cu_b was pulled out of the surface through the Coulomb attraction of O_w which pushed the top-layer Cu outwards. The E_{ads} for the dissociative adsorption was −0.53 eV, which indicates that based on thermodynamic grounds the H_2O prefers to adsorb molecularly on the top-layer W. A total electron density of 0.16 e migrated from the H_2O molecule to the surface after the dissociative adsorption, as listed in Table 3. The O_w gained 0.49e, which were donated by the Cu_b in the sub-surface layer, the W adsorption site, and H of the O_wH group. The dissociated H lost 0.62 e when bonding to the surface, whereas the O_s gained 0.26 e *via* the corresponding O_sH bond. The work function of the system was calculated at 5.33 eV, which is 0.62 eV lower than that of the dry surface, making the hydrated surface more reactive. The vibrational stretching mode of the O_wH group was calculated at 3719 cm^{-1} after hydration, *i.e.* similar to the asymmetric vibrational mode of the isolated water molecule. However, the vibrational stretching mode of the O_sH group was 3619 cm^{-1}, which is red-shifted by 38 cm^{-1} with respect to the symmetric vibrational mode after dissociation, suggesting that the O_sH bond is weaker compared to the isolated water molecule.

3.4 H_2O surface coverage

We selected the most thermodynamically favourable configurations of the single H_2O molecule adsorption system (*i.e.* with the largest negative E_{ads}) as the initial geometries to study the effect of incremental surface coverage on both the pristine (010) and reduced (101) surfaces. Both molecular and dissociative H_2O adsorption were studied for each coverage, and the configuration with the largest E_{ads} was selected to simulate the next adsorption step. The number of adsorbed H_2O molecules (n) was increased until all the potential adsorption sites were occupied, or at the onset of a second layer of H_2O.

3.4.1 Pristine (010) surface. Fig. 4 shows all the simulated H_2O coverages on the pristine (010) surface. When the surface coverage of water (C) was equal to 2.2 nm^{-2}, the two water molecules were sited at different Cu and behaved as isolated absorbates, shown in Fig. 4 as water 1 and 2. Water molecule 2 formed a single hydrogen-bond at 1.87 Å to the surface. When C increased to 4.4 nm^{-2}, four adsorbates were situated at different Cu atoms. Water 1 and 3 formed two hydrogen-bonds with O_w and O_s, whereas water 2 and 4 formed a single hydrogen-bond to O_s. When increasing C above 5.5 nm^{-2}, water 5 chemisorbed at Cu, forming two hydrogen-bonds at 2.00 and 2.09 Å with O_s, whereas water 4, located between water 1 and 5, physiosorbed onto the surface as a donor of hydrogen-bonds. The surface reached full coverage at C = 8.8 nm^{-2}, which corresponds to eight adsorbed H_2O molecules per surface simulation cell, forming an ''ice-like'' monolayer on the surface *via* a network of hydrogen-bonds interacting with O_w and O_s. Adding more H_2O molecules would lead instead to a second layer with interactions to the first H_2O monolayer on the pristine (010) $CuWO_4$ surface. The surface suffered negligible distortion at each coverage of H_2O, as only the Cu adsorption sites moved outward slightly due to Coulomb attraction.

We calculated the average Bader atomic charges of Cu, W, and O in the top layer of the (010) surface at each surface coverage of H_2O, as shown in Fig. 5. The negligible change in the Bader charges indicates that only minor amounts of electron density have migrated from the adsorbates to the surface, which is in good agreement with the small charge transfer discussed for the single H_2O molecule adsorption. The increment in the adsorption energy per H_2O molecule ($E_{\text{ads-per } H_2O}$) was calculated as a function of the coverage of H_2O. The result shows that $E_{\text{ads-per } H_2O}$ decreased from −0.89 to −0.71 eV, which indicates that single molecule adsorption is stronger than at higher coverages, although the value of $E_{\text{ads-per } H_2O}$ remained negative. We found a clear increase in the negative $E_{\text{ads-per } H_2O}$ when the surface coverage became 3.3 and 8.8 nm^{-2}, which was attributed to the formation of additional hydrogen-bonds upon adsorption of the additional water molecule, which released more energy as a result. We further calculated the surface free energies at 0 K (σ_{0K}) as a function of the coverage of H_2O at the pristine (010) surface. The steady decrease in σ_{0K} suggests that the surface–water system becomes thermodynamically more stable as the surface coverage increases. Both $E_{\text{ads-per } H_2O}$ and σ_{0K} indicate that adsorption of H_2O molecules to full monolayer coverage at the pristine (010) surface is thermodynamically feasible. However, weaker interactions between the O_w and surface were observed in the higher surface coverages. The work function at each coverage of H_2O was smaller than that of the pristine surface at 6.95 eV, suggesting that the hydrated surfaces are all more reactive than the dry one. The smallest work function of 5.94 eV was obtained at the surface coverage of 4.4 nm^{-2}, as shown in Fig. 5. This phenomenon is attributed to

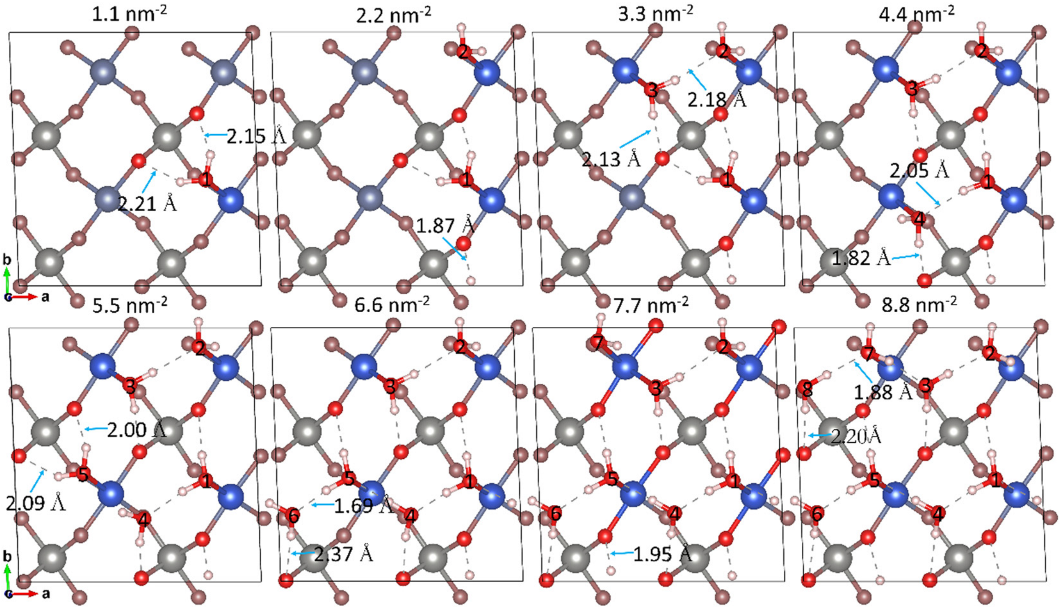

Fig. 4 Top view of H_2O coverages at the pristine (010) surface. The H_2O molecules are labelled (1 to 8) and the adsorption sites are shown highlighted in dark blue. The Cu, W, O, and H atoms are (pale and dark) blue, grey, red and white, respectively. The length of the hydrogen-bonds of the additional water molecule in each configuration is noted and shown by a blue arrow.

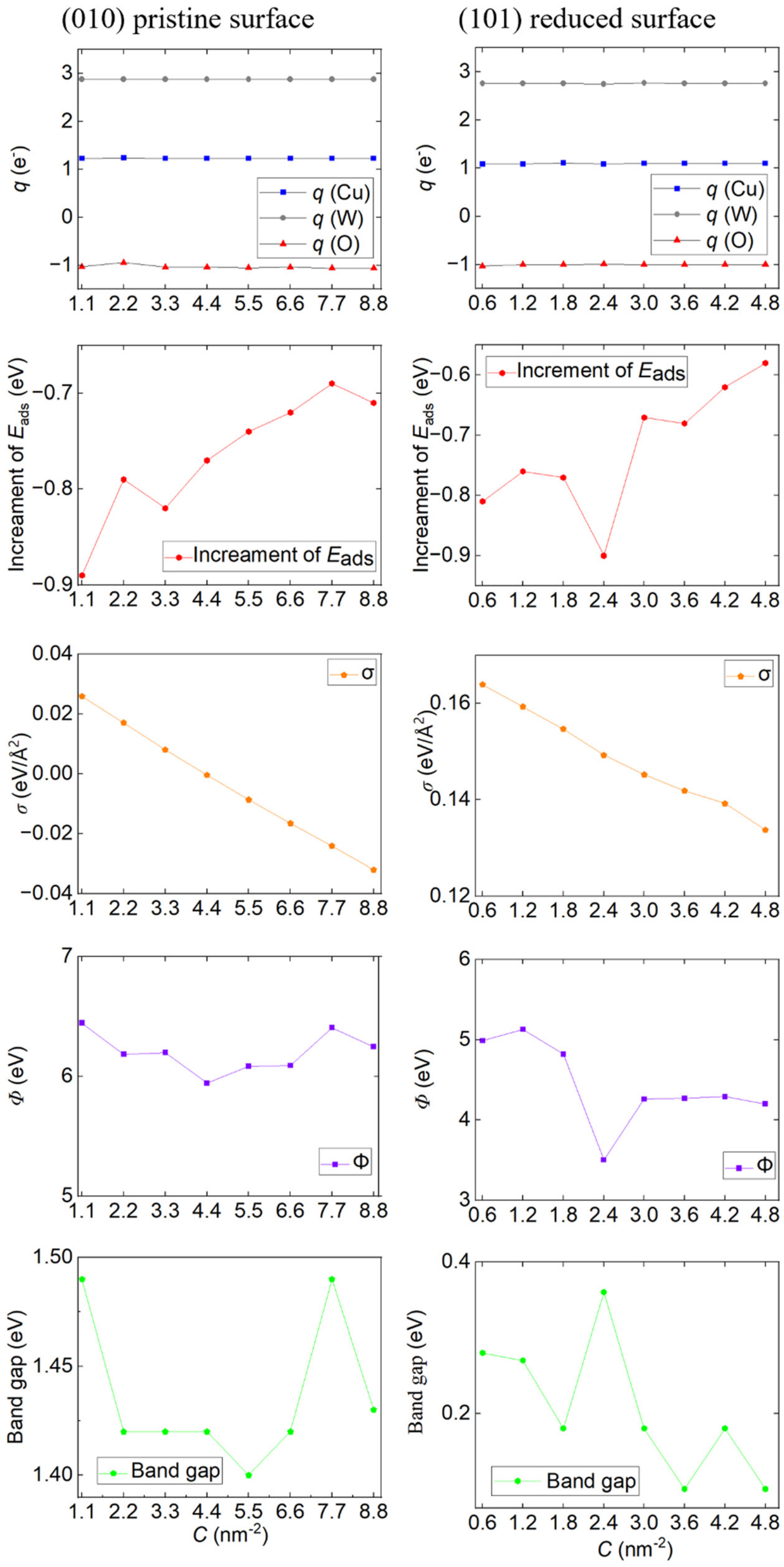

Fig. 5 Bader atomic charges (q), incremental E_{ads}, surface free energies at 0 K (σ), work functions (Φ), and band gaps at each coverage of H_2O on (left) the pristine (010) surface and (right) the reduced (101) surface.

the chemisorption of water at the Cu adsorption site when the surface coverage is less than 4.4 nm^{-2}. The electron charge migrates from the adsorbates to the surface, resulting in the lowering of the work function. When the (010) surface is hydrated to higher surface coverages above 5.5 nm^{-2}, physisorption of the additional adsorbates provides negligible electron charge to the surface, resulting in a small increase in the work function. We calculated the band gap of the hydrated system at each surface coverage, see Fig. 5. The value of the band gap fluctuates within a narrow range from 1.4 to 1.5 eV as the surface coverage is increased. The result suggests that the hydrated pristine (010) surface has the potential for photocatalytic water splitting, considering it meets the requirement of a minimum band gap of 1.23 eV for the reaction.[62]

We constructed 3D surface phase diagrams of the water adsorption for both the pristine (010) and reduced (101) surfaces. The molecular and dissociative adsorption was tested for each coverage, and the surface configuration with the lowest surface free energy, calculated based on eqn (5), was used for the construction of the phase diagrams. The 2D projections of the 3D surface phase diagrams are plotted as a function of the temperature (T) and the logarithm of the partial pressure of H_2O $\left(\log\frac{p(H_2O)}{p^0}\right)$, see Fig. 6. The curves between the intersecting energy surfaces represent the conditions required to modify the extent of H_2O adsorption.

As shown in Fig. 6, the (010) surface stays dry as the temperature increases from 300 K when the logarithm of the partial pressure of H_2O was below 8. The other five possible coverages of H_2O, *i.e.* 1.1, 3.3, 4.4, 5.5, and 6.6 nm^{-2}, are available when the partial pressure of the absorbate is increased or the temperature is lowered. The simulation slab of our surface was capable to adsorb eight H_2O molecules and reached full coverage (C) of 8.8 nm^{-2} when T was lower than 185 K and the logarithm of partial pressure of H_2O was larger than 8.6. The surface phase diagram suggests that the pristine (010) surface prefers to adsorb H_2O and reaches full coverage at a relatively low temperature or high partial pressure of this gas. Such a result is consistent with the continuously decrease in the E_{ads} per H_2O molecule as discussed in Section 3.3.1. Water adsorption on the pristine (010) surface is sensitive to the temperature and its partial pressure, as the surface coverages of 3.3 to 6.6 nm^{-2} can only be achieved in a narrow range of environmental conditions. The surface coverages of 2.2 and 7.7 nm^{-2}, corresponding to two and seven adsorbates, respectively, per simulation cell did not show in the phase diagram, as they are inaccessible.

3.4.2 Reduced (101) surface. The multiple H_2O adsorptions at the reduced (101) surface are shown in Fig. 7. When the coverage of H_2O was 0.012 nm^{-2}, water 1 and 2 behaved as isolated adsorbates, interacting molecularly with separate W and O_s ions. When the surface coverage was 1.8 nm^{-2}, water 3 dissociated owing to the larger E_{ads} than for the molecular adsorption. The O_wH group migrated to the sub-surface and coordinated Cu_b. The dissociated H bonded with O_s in the top layer, forming a hydrogen-bond at 1.80 Å. As C is increased to 2.4 nm^{-2}, water 4 coordinated W molecularly, forming a hydrogen-bond of 1.76 Å and at a coverage of 3.0 nm^{-2}, all the H_2O molecules were adsorbed molecularly onto the surface. Water 1 to 4 coordinated to W sites behaved as isolated adsorbates, forming a single hydrogen-bond to the surface between 1.81 to 2.01 Å. Water 5 interacted with Cu_b in the sub-surface layer at the O vacancy, forming hydrogen-bonds with neighbouring O_s at 1.75 Å and O_w at 1.88 Å. When C was 3.6 nm^{-2}, we found that water 6 coordinated Cu_b in the top-layer of the surface and formed a hydrogen-bond with the neighbouring O_w of 1.82 Å. Water 7 adsorbed at the Cu site in the top layer, interacting with the neighbouring O_w and O_s at 1.92 and 1.93 Å, respectively. When C increased to 4.8 nm^{-2}, the reduced (101) surface accommodated eight H_2O molecules and reached full coverage. Water 1 to 4 adsorbed at W as isolated adsorbates, whereas water 5 to 8 coordinated Cu. All the adsorbates interacted with neighbouring O as the donor and acceptor of hydrogen-bonds of between 1.74 to 1.96 Å, forming an "ice-like" monolayer. We did not find evidence of H_2O molecule dissociation at any of the explored adsorption sites, and additional water molecules would form instead a second monolayer of H_2O on the reduced (101) surface.

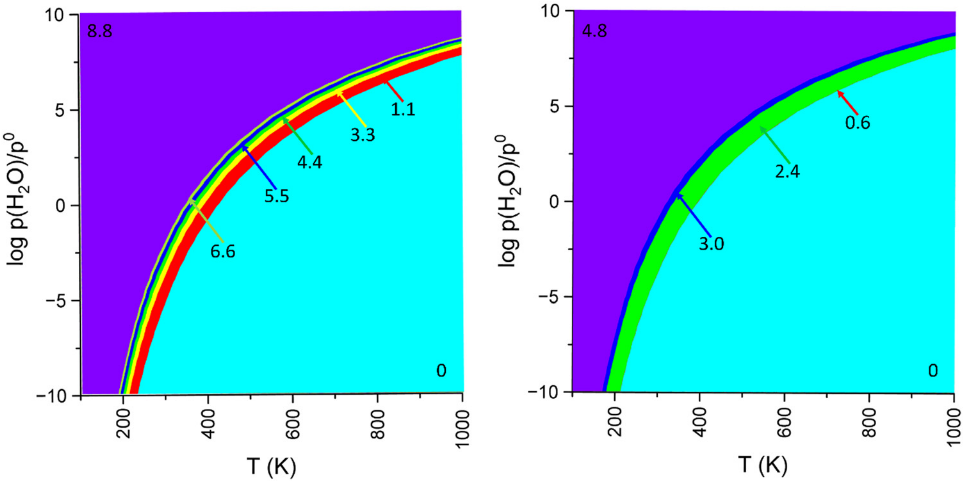

Fig. 6 Surface phase diagrams of (left) the pristine (010) surface and (right) the reduced (101) surface as a function of the temperature (T) and the logarithm of partial pressure of H_2O ($\log p(H_2O)/p^0(H_2O)$). The coverage (C) of adsorbed H_2O (unit: nm^{-2}) are noted in the figure.

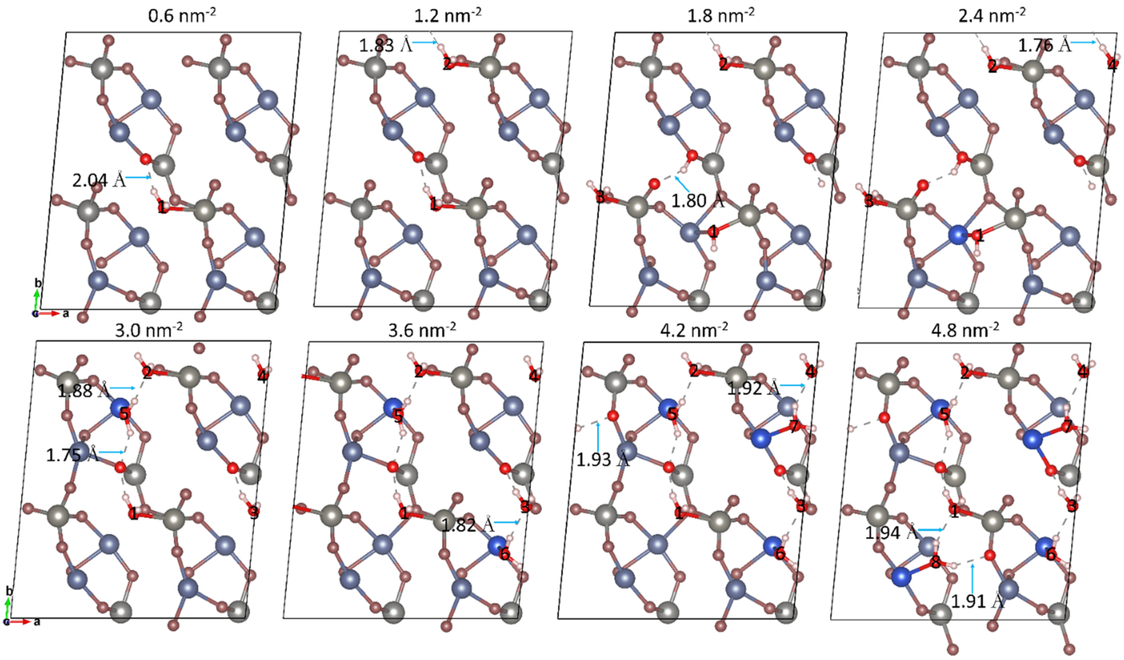

Fig. 7 Top view of H_2O coverages at the reduced (101) surface. The H_2O molecules are labelled (1 to 8) and the adsorption sites are shown highlighted in dark blue. The Cu, W, O, and H atom are (dark and pale) blue, grey, red and white, respectively. The length of the hydrogen-bonds of the additional water molecule in each configuration is noted and shown by a blue arrows.

The average Bader atomic charges of Cu, W, and O in the top-layer of the reduced (101) surface for each surface coverage were calculated, as shown in Fig. 5. Negligible changes of the average Bader charge were obtained after hydration, suggesting that only small amounts of electron density were transferred from the adsorbates to the surface, which agrees with the result for the single water adsorption at the reduced (101) surface. The $E_{\text{ads-per } H_2O}$ of the reduced (101) surface decreased from −0.93 to −0.43 eV with increasing surface coverage of water, which indicates that the interaction between the adsorbates and surface was weaker at higher surface coverages. A substantial reduction of $E_{\text{ads-per } H_2O}$ was observed at the surface coverages of 2.4 nm^{-2}, owing to the formation of a Cu_b–O_w bond between Cu_b in the sub-surface and the O_wH group, resulting in the release of more energy. The σ_{0K} decreased with water coverage, suggesting that the reduced (101) surface prefers to reach full coverage which is more thermodynamically favourable. As shown in Fig. 5, a substantial lowering of the work function was observed after hydration compared to 7.59 eV of the dry (101) surface, due to more electron charge made available by the adsorbates, indicating that the hydrated systems are more reactive than the dry surface, especially for its lowest value of 3.50 eV at the surface coverage of 2.4 nm^{-2}. The band gaps of the hydrated systems at each surface coverage were calculated and are shown in Fig. 5. The results suggests that the reduced (101) surface is not suitable for photocatalytic water splitting, given that its band gap is significantly smaller than 1.23 eV at any water coverage.[62]

We constructed the surface phase diagram as a function of the temperature and partial pressure of H_2O on the reduced (101) surface, as shown in Fig. 6. The surface stayed dry when the temperature was above 200 K and the logarithm of the partial pressure of H_2O was below 7. The surface reached full hydration at a high partial pressure of H_2O and high temperature, corresponding to a surface coverage equal to 4.8 nm^{-2}. The other three regions of coverage, where C is equal to 0.6, 2.4 and 3.0 nm^{-2} were also shown in the phase diagram. The results suggest that the reduced (101) surface is sensitive to the environment as it prefers to stay dry, or fully hydrated under most environmental conditions. The other possible surface coverages of water could only be reached in a narrow range of temperatures and partial pressures of H_2O. The H_2O coverages of 1.2, 1.8 3.6, and 4.2 nm^{-2} do not show in the phase diagram since they are inaccessible.

4. Conclusions

In this paper, we have reported a computational study based on the density functional theory of the adsorption of water on the pristine (010) and reduced (101) surfaces of $CuWO_4$. On the pristine (010) surface, the adsorption mode with H_2O coordinating Cu in the μ_3–η^3 configuration has the largest adsorption energy of −0.89 eV. At the reduced (101) surface, the H_2O molecule preferentially adsorbs over W with an adsorption energy of −0.81 eV, forming a μ_2–η^2 configuration. Following single-molecule adsorption, we next investigated adsorption of multiple H_2O molecules on the pristine (010) and reduced (101) surfaces, starting from the most favourable adsorption modes obtained for the single H_2O molecule. We found that the pristine (010) surface can adsorb up to eight H_2O molecules per surface cell. Four H_2O molecules coordinated Cu in the surface, whereas the other four interacted with neighbouring H_2O molecules *via* hydrogen-bonds, forming an ice-like monolayer over the surface. The reduced (101) surface adsorbed eight H_2O molecules before it achieved full coverage. Four H_2O molecules coordinated W as isolated adsorbates, two H_2O molecules coordinated Cu in the sub-surface, whereas two H_2O molecules interacted with Cu in the top-layer.

The electronic properties were calculated for both surfaces. We found only negligible change in the Bader atomic charges of Cu, W, and O upon water adsorption, which is consistent with the minor charge transfer observed for the single molecule adsorption systems. The work functions of both hydrated surfaces are smaller than the dry surfaces at all coverages. The band gap of the hydrated (010) surface at each surface coverage fluctuates within 0.1 eV, and all are above 1.23 eV, which shows potential for its utilization in photocatalytic water splitting. However, the band gap of the reduced (101) surface at each surface coverage is well below 1.23 eV, which makes it an unlikely candidate for photocatalytic water splitting. The surface phase diagram of the pristine (010) and reduced (101) surfaces were obtained as a function of the temperature and partial pressure of H_2O. The results suggest that the two surfaces prefer to remain dry at low partial pressures of H_2O but can become fully hydrated at high partial pressures of H_2O and at low temperatures. Other coverages, although shown in the phase diagram, were hard to achieve due to the narrow range of temperature and H_2O partial pressure required. In summary, our results show that the pristine (010) surface of $CuWO_4$ has the potential to be utilized in photocatalytic water splitting, which will be the focus of future work.

Data availability

All the data supporting the findings of this study are provided within the paper and in the ESI† file.

Conflicts of interest

The authors have no conflict of interest to declare.

Acknowledgements

XC is grateful to the University of Leeds for the provision of a Research Scholarship. *Via* our membership of the UK's HEC Materials Chemistry Consortium, which is funded by EPSRC (EP/X035859), this work made use of the ARCHER2 UK National Supercomputing Service (**https://www.archer2.ac.uk**). This research has also used ARC4, part of the High-Performance Computing facilities at the University of Leeds, UK. For the purpose of Open Access, the authors have applied a CC BY public copyright licence to any Author Accepted Manuscript version arising from this submission.

References

1 D. Feldman, V. Ramasamy, R. Fu, A. Ramdas, J. Desai and R. Margolis, *U.S. Solar Photovoltaic System and Energy Storage Cost Benchmark: Q1 2020*, 2020.

2 N. Kannan and D. Vakeesan, *Renewable Sustainable Energy Rev.*, 2016, **62**, 1092–1105.

3 D. Feldman, V. Ramasamy, R. Fu, A. Ramdas, J. Desai and R. Margolis, *U.S. Solar Photovoltaic System and Energy Storage Cost Benchmark: Q1 2020*, 2020.

4 K. Honda, One and Two-dimensional Structure of Alpha-Helix and Beta-Sheet Forms of Poly(L-Alanine) shown by Specific Heat Measurements at Low Temperatures (1.5–20 K), *Nature*, 1910, **238**, 38–40.

5 Y. Li and S. C. E. Tsang, Recent progress and strategies for enhancing photocatalytic water splitting, *Mater. Today Sustainability*, 2020, **9**, 100032.

6 K. Maeda, Photocatalytic water splitting using semiconductor particles, *J. Photochem. Photobiol., C*, 1996, **96**, 1825–2236.

7 K. Takanabe, Photocatalytic Water Splitting: Quantitative Approaches toward Photocatalyst by Design, *ACS Catal.*, 2017, **7**, 8006–8022.

8 N. Serpone, *Kirk-Othmer Encyclopedia of Chemical Technology*, Wiley, 2000.

9 K. Maeda and K. Domen, Photocatalytic Water Splitting: Recent Progress and Future Challenges, *J. Phys. Chem. Lett.*, 2010, **1**, 2655–2661.

10 E. Zaki, F. Mirabella, F. Ivars-Barceló and J. Seifert, *et al.*, Water adsorption on the $Fe_3O_4(111)$ surface: dissociation and network formation, *Phys. Chem. Chem. Phys.*, 2018, **20**, 15764–15774.

11 E. Zaki, F. Mirabella, F. Ivars-Barceló, J. Seifert and S. Carey, *et al.*, Water adsorption on the $Fe_3O_4(111)$ surface: dissociation and network formation, *Phys. Chem. Chem. Phys.*, 2018, **20**, 15764–15774.

12 A. Calzolari and A. Catellani, Water adsorption on nonpolar ZnO(1010) surface: a microscopic understanding, *J. Phys. Chem. C*, 2009, **113**, 2896–2902.

13 J. J. Calvin, P. F. Rosen and N. L. Ross, *et al.*, Review of surface water interactions with metal oxide nanoparticles, *J. Mater. Res.*, 2019, **34**, 416–427.

14 R. Mu, Z. J. Zhao, Z. Dohnálek and J. Gong, Structural motifs of water on metal oxide surfaces, *Chem. Soc. Rev.*, 2017, **46**, 1785–1806.

15 L. Wang, C. Shi, L. Pan, X. Zhang and J. J. Zou, Rational design, synthesis, adsorption principles and applications of metal oxide adsorbents: a review, *Nanoscale*, 2020, **12**, 4790–4815.

16 U. Qumar, J. Z. Hassan and R. A. Bhatti, et,al, Photocatalysis vs adsorption by metal oxide nanoparticles, *J. Mater. Sci. Technol.*, 2022, **131**, 122–166.

17 A. Hodgson and S. Haq, Water adsorption and the wetting of metal surfaces, *Surf. Sci. Rep.*, 2009, **64**, 381–451.

18 M. Sacchi and A. Tamtögl, Water adsorption and dynamics on graphene and other 2D materials: computational and experimental advances, *Adv. Phys. X*, 2023, **8**, 2134051.

19 M. J. Ungerer, D. Santos-Carballal, A. Cadi-Essadek, C. G. C. E. Van Sittert and N. H. De Leeuw, Interaction of H2O with the Platinum Pt (001), (011), and (111) Surfaces: A Density Functional Theory Study with Long-Range Dispersion Corrections, *J. Phys. Chem. C*, 2019, **45**, 27465–27476.

20 H. Eidsvåg, S. Bentouba, P. Vajeeston and S. Yohi, *et al.*, TiO_2 as a Photocatalyst for Water Splitting—An Experimental and Theoretical Review, *Molecules*, 2021, **26**, 1687.

21 J. Kegel, I. M. Povey and M. E. Pemble, Zinc oxide for solar water splitting: a brief review of the material's challenges and associated opportunities, *Nano Energy*, 2018, **54**, 409–428.

22 M. B. Costa, M. A. de Araújo and M. V. de L. Tinoco, *et al.*, Current trending and beyond for solar-driven water splitting reaction on WO_3 photoanodes, *J. Energy Chem.*, 2022, **73**, 88–113.

23 P. Raizada, S. Sharma, A. Kumar and P. Singh, *et al.*, Performance improvement strategies of $CuWO_4$ photocatalyst for hydrogen generation and pollutant degradation, *J. Environ. Chem. Eng.*, 2020, **8**, 104230.

24 Y. Tang, N. Rong, F. Liu and M. Chu, *et al.*, Enhancement of the photoelectrochemical performance of $CuWO_4$ films for water splitting by hydrogen treatment, *Appl. Surf. Sci.*, 2016, **361**, 133–140.

25 K. J. Pyper, J. E. Yourey and B. M. Bartlett, Reactivity of $CuWO_4$ in photoelectrochemical water oxidation is dictated by a midgap electronic state, *J. Phys. Chem. C*, 2013, **117**, 24726–24732.

26 Y. Liu, L. Chen and X. Zhu, *et al.*, Effects of operating temperature on photoelectrochemical performance of $CuWO_4$ film photoanode, *J. Electroanal. Chem.*, 2022, **924**, 116859.

27 L. Kihlborg and E. Gebert, $CuWO_4$, a distorted Wolframite-type structure, *Acta Crystallogr., Sect. B: Struct. Crystallogr. Cryst. Chem.*, 1970, **26**, 1020–1026.

28 X. Chu, D. Santos-Carballal and N. H. de Leeuw, Exploring the Redox Properties of the Low-Miller Index Surfaces of Copper Tungstate ($CuWO_4$): Evaluating the Impact of the Environmental Conditions on the Water Splitting and Carbon Dioxide Reduction Processes, *J. Phys. Chem. C*, 2023, **127**, 18944–18961.

29 J. E. Yourey and B. M. Bartlett, Electrochemical deposition and photoelectrochemistry of $CuWO_4$, a promising photoanode for water oxidation, *J. Mater. Chem.*, 2011, **21**, 7651–7660.

30 K. Li, C. Zhang and X. Li, *et al.*, A nanostructured $CuWO_4/Mn_3O_4$ with p/n heterojunction as photoanode toward enhanced water oxidation, *Catal. Today*, 2019, **335**, 173–179.

31 Z. Lu and Z. Wang, S-scheme $CuWO_4$@g-C_3N_4 core-shell microsphere for CO_2 photoreduction, *Mater. Sci. Semicond. Process.*, 2023, **153**, 107177.

32 J. E. Yourey and B. M. Bartlett, Electrochemical deposition and photoelectrochemistry of $CuWO_4$, a promising photoanode for water oxidation, *J. Mater. Chem.*, 2011, **21**, 7651–7660.

33 T. Wang, X. Fan, B. Gao and C. Jiang, *et al.*, Self-Assembled Urchin-Like $CuWO_4/WO_3$ Heterojunction Nanoarrays as Photoanodes for Photoelectrochemical Water Splitting, *ChemElectroChem*, 2021, **8**, 125–134.

34 A. C. Catto, T. Fiorido and É. L. S. Souza, *et al.*, Improving the ozone gas-sensing properties of $CuWO_4$ nanoparticles, *J. Alloys Compd.*, 2018, **748**, 411–417.

35 Y. Liu, L. Chen and X. Zhu, *et al.*, Effects of operating temperature on photoelectrochemical performance of $CuWO_4$ film photoanode, *J. Electroanal. Chem.*, 2022, **924**, 116859.

36 P. Raizada, S. Sharma and A. Kumar, *et al.*, Performance improvement strategies of $CuWO_4$ photocatalyst for hydrogen generation and pollutant degradation, *J. Environ. Chem. Eng.*, 2020, **8**, 104230.

37 C. M. Tian, M. Jiang and D. Tang, *et al.*, Elucidating the electronic structure of $CuWO_4$ thin films for enhanced photoelectrochemical water splitting, *J. Mater. Chem. A*, 2019, **7**, 11895–11907.

38 G. Kresse and J. Hafner, Ab. initio molecular dynamics for liquid metals, *Phys. Rev. B: Condens. Matter Mater. Phys.*, 1993, **47**, 558.

39 G. Kresse, Ab initio molecular-dynamics simulation of the liquid-metal-amorphous-semiconductor transition in germanium, *Phys. Rev. B: Condens. Matter Mater. Phys.*, 1994, **8**, 14251.

40 G. Kresse and J. Furthmü, Efficient iterative schemes for ab initio total-energy calculations using a plane-wave basis set, *Phys. Rev. B: Condens. Matter Mater. Phys.*, 1996, **54**, 11169.

41 J. P. Perdew, K. Burke and M. Ernzerhof, Generalized Gradient Approximation Made Simple, *Phys. Rev. Lett.*, 1996, **77**, 3865.

42 S. Grimme, Semiempirical GGA-type density functional constructed with a long-range dispersion correction, *J. Comput. Chem.*, 2006, **27**, 1787–1799.

43 T. Suter, E. G. Webb, H. Böhni and R. C. Alkire, Pit Initiation on Stainless Steels in 1 M NaCl With and Without Mechanical Stress, *J. Electrochem. Soc.*, 2001, **148**, B174.

44 S. L. Dudarev, G. A. Botton and S. Y. Savrasov, *et al.*, Electron-energy-loss spectra and the structural stability of nickel oxide: an LSDAU study, *Phys. Rev. B: Condens. Matter Mater. Phys.*, 1998, **57**, 1505.

45 D. J. Chadi, Special points for Brillouin-zone integrations, *Phys. Rev. B: Condens. Matter Mater. Phys.*, 1977, **16**, 1746.

46 D. Sheppard, R. Terrell and G. Henkelman, Optimization methods for finding minimum energy paths, *J. Chem. Phys.*, 2008, **128**, 134106.

47 P. W. Tasker, The stability of ionic crystal surfaces, *Solid State Phys.*, 1979, **12**, 4977–4984.

48 G. W. Watson, T. Kelsey and N. H. De Leeuw, *et al.*, Atomistic simulation of dislocations, surfaces and interfaces in MgO, *J. Chem. Soc.*, 1996, **92**, 433–438.

49 P. E. Blochl, O. Jepsen and O. K. Andersen, Improved tetrahedron method far Brilleuin-zane integratians, *Phys. Rev. B: Condens. Matter Mater. Phys.*, 1994, **94**, 16223.

50 M. W. Chase, Jr., NIST-JANAF Thermochemical Tables, Fourth Edition, *J. Phys. Chem. Ref. Data*, 1998, 1–1951.

51 D. Santos-Carballal and N. H. de Leeuw, Catalytic formation of oxalic acid on the partially oxidised greigite Fe_3S_4(001) surface, *Phys. Chem. Chem. Phys.*, 2022, **24**, 20104–20124.

52 G. Henkelman, A. Arnaldsson and H. Jónsson, A fast and robust algorithm for Bader decomposition of charge density, *Comput. Mater. Sci.*, 2006, **36**, 354–360.

53 W. Tang, E. Sanville and G. Henkelman, A grid-based Bader analysis algorithm without lattice bias, *J. Phys.: Condens. Matter*, 2009, **21**, 8.

54 B. Ramogayana, D. Santos-Carballal and K. P. Maenetja, A DFT+*U*-D3 Study of the Adsorption of Hydrogen Fluoride and Ethylene Carbonate on the Niobium-Doped (001), (011), and (111) Surfaces of Lithium Manganese Oxide, *J. Electrochem. Soc.*, 2022, **169**, 090507.

55 J. Tersoff and D. R. Hamann, Theory of the scanning tunneling microscope, *Phys. Rev. B: Condens. Matter Mater. Phys.*, 1985, **31**, 805.

56 D. E. P. Vanpoucke and G. Brocks, Formation of Pt-induced Ge atomic nanowires on Pt/Ge(001): a density functional theory study, *Phys. Rev. B: Condens. Matter Mater. Phys.*, 2008, **77**, 241308.

57 A. R. Hoy and P. R. Bunker, A Precise Solution of the Rotation Bending Schrbdinger Equation for a Triatomic Molecule wiih Application to the Water Molecule, *J. Mol. Spectrosc.*, 1979, **74**, 1–8.

58 G. Herzberg and K. P. Huber, *Molecular spectra and molecular structure*, Springer US, Boston, MA, 1979, pp. 8–689.

59 T. Shimanouchi, H. Matsuura, Y. Ogawa and I. Harada, Tables of molecular vibrational frequencies, *J. Phys. Chem. Ref. Data*, 1978, **7**, 1323–1444.

60 D. H. Gibson, The Organometallic Chemistry of Carbon Dioxide, *Chem. Rev.*, 1996, **96**, 2063–2096.

61 D. H. Gibson, Carbon dioxide coordination chemistry: metal complexes and surface-bound species, *Coord. Chem. Rev.*, 1999, **185**, 335–355.

62 B. Huang and J. N. Hart, DFT study of various tungstates for photocatalytic water splitting, *Phys. Chem. Chem. Phys.*, 2020, **22**, 1727–1737.